

Article

Crosstalk Reduction in Voxels for a See-Through Holographic Waveguide by Using Integral Imaging with Compensated Elemental Images

Jiwoon Yeom *, Yeseul Son and Kwangsoon Choi

Korea Electronics Technology Institute, World Cup buk-ro 54-gil, Mapo-gu, Seoul 03924, Korea; yeseul0323@keti.re.kr (Y.S.); lenon@keti.re.kr (K.C.)

* Correspondence: jiwoon.yeom@keti.re.kr

Abstract: The representation of three-dimensional volumetric pixels, voxels, is an important issue for the near-to-eye displays (NEDs) to solve the vergence-accommodation conflict problem. Although the holographic waveguides using holographic optical element (HOE) couplers are promising technologies for NEDs with the ultra-thin structure and high transparency, most of them have presented only a single and fixed depth plane. In this paper, we analyze the imaging characteristics of holographic waveguides, particularly to represent the arbitrary voxels and investigate the voxel duplication problem arising from the non-collimated light from the voxels. In order to prevent the image crosstalk arising from the voxel duplication, we propose an adjustment method for the emission angle profile of voxels by using the integral imaging technique. In the proposed method, the sub-regions of elemental images, which correspond to the duplicated voxels, are masked in order to optimize the emission angle of integrated voxels. In the experimental verification, a see-through integral imaging system, based on the organic light-emitting diode display and a holographic waveguide with the thickness of 5 mm, was constructed. The fabricated HOE in the waveguide showed high diffraction efficiency of 72.8 %, 76.6%, and 72.5 % for 460 nm, 532 nm, and 640 nm lasers, respectively. By applying the masked elemental images, the proposed method resulted in a reduced crosstalk in the observed voxels by 2.35 times. The full-color experimental results of see-through holographic waveguide with integral imaging are provided, whereby the observed 3D images are presented clearly without the ghost images due to the voxel duplication problem.

Keywords: holographic waveguide; integral imaging; see-through display; augmented reality; autostereoscopy



Citation: Yeom, J.; Son, Y.; Choi, K. Crosstalk Reduction in Voxels for a See-Through Holographic Waveguide by Using Integral Imaging with Compensated Elemental Images. *Photonics* **2021**, *8*, 217. <https://doi.org/10.3390/photonics8060217>

Received: 22 April 2021

Accepted: 6 June 2021

Published: 11 June 2021

Publisher's Note: MDPI stays neutral with regard to jurisdictional claims in published maps and institutional affiliations.



Copyright: © 2021 by the authors. Licensee MDPI, Basel, Switzerland. This article is an open access article distributed under the terms and conditions of the Creative Commons Attribution (CC BY) license (<https://creativecommons.org/licenses/by/4.0/>).

1. Introduction

See-through near-to-eye displays (NEDs), which are core components of the augmented reality (AR) headsets, have been given considerable attention recently [1,2]. Various optical technologies have been actively studied for the see-through AR NEDs, such as the free-form optics [3], the direct retinal projection optics [4,5], and the waveguide optics [6–15]. Among these technologies, the waveguide optics provide the best way to minimize the size of NEDs, which is crucial for the comfort and compactness of the AR headsets. Waveguide technologies can be categorized into three groups according to the types of couplers: geometric waveguides with the reflective couplers [6–8], the diffractive waveguide with the surface relief grating couplers [9], and the holographic waveguide with the holographic optical element (HOE) couplers [10–15].

Among them, the holographic waveguides are the most promising techniques, since the HOE couplers provide benefits, including having an extremely thin structure, as well as high transparency compared to the other types of couplers. The HOE couplers are typically fabricated using thin photopolymer films, and diffract an incident wave into the pre-defined wave-front, when it satisfies the Bragg condition of the volume hologram. On

the other hand, most natural light from the real-world, which deviates from the Bragg condition, passes through the HOEs without diffraction. Such a selective functionality of HOEs allows users to view a real-world scene more clearly without severe light attenuation or degradation.

Among the key features in ensuring NEDs are widespread in the market is in providing the correct depth cues, including the accommodation effects for the virtual images. The vergence-accommodation conflict (VAC), which represents a mismatch between the vergence distance and focal distance of human eye [16], may lead to visual discomfort, eye fatigue, and nausea. Unfortunately, for holographic waveguides, most studies have focused on presenting the virtual images at optical infinity [10–12], which causes the VAC problem. In this case, the waveguide structure and HOEs are optimized for the collimated light source. The collimated ray bundles in the holographic waveguide do not deliver information for the correct depth cues, which makes it more difficult to represent the three-dimensional (3D) pixels, known as voxels, at the arbitrary depths. In a few studies, holographic display technologies were adopted with the holographic waveguide, in order to induce the accommodation effects [14,15]. However, in previous studies, the resultant 3D images suffered from monochrome and small virtual images. The holographic displays in these studies were based on the monochrome plane wave illumination with a small diffraction angle. Therefore, a thorough analysis was not conducted regarding the imaging characteristics of a holographic waveguide for a practical light source with the non-collimation and broadband spectrum.

In this paper, we analyze the imaging characteristics of holographic waveguides to represent voxels with a broad spectrum of light, and propose an adjustment method for the emission angle of voxels, in order to present them without the ghost images. For adjusting and optimizing the emission angle of voxels, we adopted the integral imaging (InIm) technique, one of the representative autostereoscopic technologies, with the compensated elemental images (EIs). In Section 2, the imaging properties of holographic waveguides are investigated in view of adopting a non-collimated light source. Additionally, the voxel duplication problem is analyzed, which arises from the large emission angle of each voxel. In order to suppress the ghost images of 3D contents arising from the voxel duplication, the InIm system based on the lenslet-array adjusts the emission angle of each voxel by using the EIs compensation method. In Section 3, we present a holographic waveguide prototype with high diffraction efficiency (DE), and examine the optical properties of the fabricated HOE coupler. The displaying experiments using the fabricated holographic waveguide and InIm system validate the proposed method, which presents the voxels in 3D contents without the ghost images.

2. Principles

2.1. Voxel Duplication Problem in Holographic Waveguide

Figure 1 presents a schematic of the voxel representation in a holographic waveguide where the unintended duplication of voxels occurs. For the holographic waveguide with the periodic volume gratings, a single voxel with the distance of $|z_v|$ from the in-coupler was considered. The voxel emits the diverging spherical wave with a large emission angle (θ_e) and broad spectrum. The only limited portion of θ_e is incident on the waveguide by the diffraction at the in-coupler. In Figure 1, $\theta_{in,ub}$ and $\theta_{in,lb}$ denote the upper and lower bounds for the portion of light, respectively, which may be in-coupled into the waveguide, in the perspective of the angle of incidence (AOI).

For the light rays within the angular range of $\theta_{in,ub}$ and $\theta_{in,lb}$, the relationship between the incident angle and diffracted angle with the Bragg diffraction at the in-coupler is expressed as Equation (1) [17].

$$\theta_+ = \theta_- + 2\zeta, \quad (1)$$

where ζ is the grating slanted angle of volume grating, and θ_- and θ_+ represent the incident angle and diffracted angle of light rays at the HOE, respectively. Note that the relationship

of Equation (1) is valid, when the wavelength of incident wave (λ) satisfies the Bragg condition as expressed in Equation (2).

$$\lambda = 2n_r\Lambda \cdot \cos(\xi + \theta_-), \tag{2}$$

where n_r is the refractive index of photopolymer, and Λ is the grating period of volume grating.

The duplication of imaged voxel arises from the large and non-optimized emission angle for each voxel. Supposing most out-coupled lights form a desirable image of voxel after n -th total internal reflections (TIRs) in the waveguide, we define the AOIs of rays satisfying this condition as an effective angular range (EAR). The EAR corresponds to the AOIs between $\theta_{eff,lb}$ and $\theta_{eff,ub}$ in Figure 1. The light whose AOI on the waveguide is smaller than $\theta_{eff,lb}$ is out-coupled from the waveguide after undergoing $(n + 2)$ -th TIRs. Similarly, the light with the larger AOI than $\theta_{eff,ub}$ is out-coupled after $(n - 2)$ -th TIRs, although it is not drawn in Figure 1. These two or more groups of light provide different images of voxels, whereas they originate from the common point light source at (x_v, z_v) . An observer perceives one intended image of voxel, and one or more duplicated images of it. In this paper, we refer to this as the voxel duplication problem. The voxel duplication problem leads to a crosstalk of 3D images, and deteriorates the quality of provided virtual images.

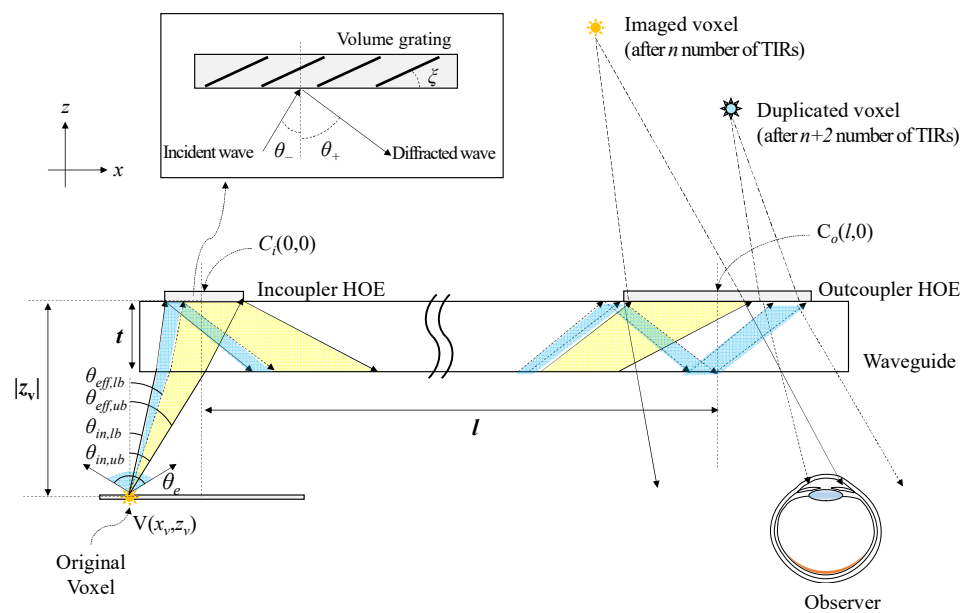


Figure 1. The schematic diagram for the voxel duplication problem in the holographic waveguide with the arbitrary voxels, which emit the non-collimated light with the large emission angle.

The detailed trajectory of propagated light in the waveguide can be investigated easily by stacking up virtual waveguides according to the number of TIRs [18]. Figure 2 shows a stacked virtual waveguide model for analyzing the ray trajectory according to the TIRs. Two virtual out-couplers are illustrated at the coordinate of (l, nt) and $(l, (n + 2)t)$, which correspond to the destination of propagated rays after the n -th and $(n + 2)$ -th TIRs, respectively. Since the rays whose AOI on the waveguide is smaller than $\theta_{eff,lb}$ do not reach the out-coupler during the n -th TIRs, they pass through the virtual out-coupler at (l, nt) in Figure 2, and encounter the virtual out-coupler at $(l, (n + 2)t)$. For the virtual out-coupler at (l, nt) , the ray passing through the leftmost position of it is the criteria to determine the contributive rays to the voxel duplication problem.

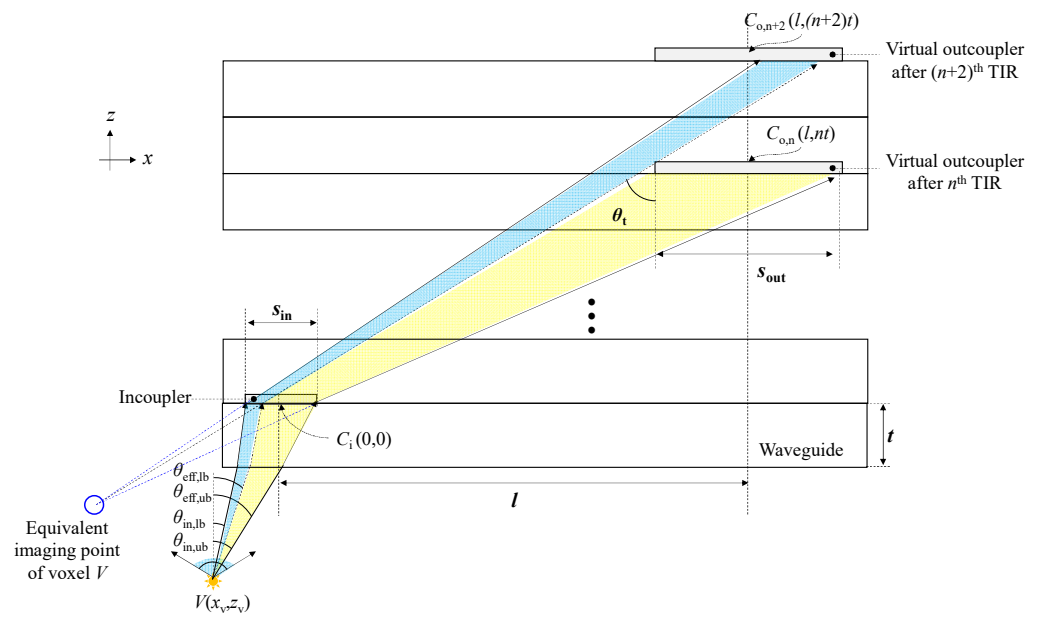


Figure 2. The trajectory of propagated rays by TIRs, which originate from the voxel V , in the holographic waveguide. We illustrate the virtual waveguide models as being stacked up for the intuitive investigation of ray trajectory according to the multiple TIRs.

In order to derive a propagation angle (θ_t) for the criteria of voxel duplication problem, we adopted the concept of equivalent imaging points, as proposed in Ref. [18]. The equivalent imaging point denotes the converging point of set of rays, when one extends the propagated rays with the TIRs in the waveguide. When one retraces the bundle of rays diffracted at the in-coupler, a crossing point of them determines the equivalent imaging point of the voxel. In this paper, we approximated the equivalent imaging point of the voxel into a crossing point of extended lines for marginal rays diffracted at the in-coupler. If we represent the equivalent imaging point of the voxel as V_e , the location of V_e is expressed as below:

$$\begin{cases} z_{ev} = -s_{in} \times \left[\tan\left(\sin^{-1}\left(\frac{1}{n_r} \sin \theta_{in,ub}\right) + 2\zeta\right) - \tan\left(\sin^{-1}\left(\frac{1}{n_r} \sin \theta_{in,lb}\right) + 2\zeta\right) \right]^{-1} \\ x_{ev} = z_{ev} \times \tan\left(\sin^{-1}\left(\frac{1}{n_r} \sin \theta_{in,lb}\right) + 2\zeta\right) - \frac{s_{in}}{2} \end{cases}, \quad (3)$$

where x_{ev} and z_{ev} represent the coordinates of V_e , and s_{in} represents the width of the in-coupler. Using the position of V_e , we derived the criteria for the voxel duplication problem in view of the propagation angle (θ_t).

$$\theta_t = \tan^{-1}\left(\frac{l - s_{out}/2 - x_{ev}}{nt - z_{ev}}\right), \quad (4)$$

where l , t , and s_{out} represent the distance between the in-coupler and out-coupler, thickness of waveguide, and width of out-coupler.

Since the light ray with the AOI of $\theta_{eff,lb}$ is diffracted into the light ray with the propagation angle of θ_t , we rewrote θ_t as below.

$$\theta_t = \sin^{-1}\left(\frac{1}{n_r} \sin \theta_{eff,lb}\right) + 2\zeta. \quad (5)$$

From Equations (4) and (5), $\theta_{eff,lb}$ is given by Equation (6).

$$\theta_{eff,lb} = \sin^{-1} \left(n_r \cdot \sin \left(\tan^{-1} \left(\frac{l - s_{out}/2 - x_{ev}}{nt - z_{ev}} \right) - 2\zeta \right) \right). \tag{6}$$

The ray bundles whose AOIs are smaller than $\theta_{eff,lb}$ lead to another imaged voxel due to different optical path lengths during the additional TIRs. Although we derived the condition for the voxel duplication problem between the n -th and $(n + 2)$ -th TIRs cases, the aforementioned analysis is easily extended to the case of other numbers of TIRs by replacing n in Equation (6) accordingly.

Figure 3a,b show simulation results for the observed voxels through the holographic waveguide with the configuration depicted in Figure 1. In the simulation, we assumed three equidistantly positioned voxels (the angular distance of 10°) with the broad-spectrum light. The depths of voxels were 400 mm in Figure 3a, and 4000 mm in Figure 3b. The specifications of the holographic waveguide, such as the thickness ($t = 5.0$ mm), the distance between the in-coupler and out-coupler ($l = 62.5$ mm), and the grating slanted angle ($\zeta = 27.5^\circ$), were identical to those in the experiments, as discussed in Section 3.1.

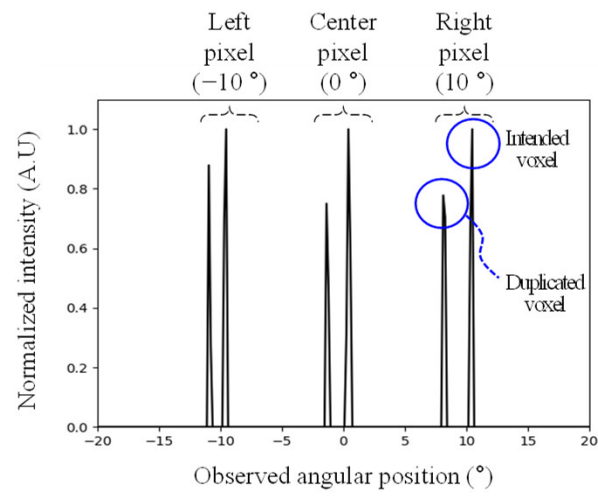
In Figure 3a with the $z_v = -400$ mm condition, there are two peaks for each voxel, which represent the voxel duplication problem arising from the large and non-optimized emission angle. The secondary peak for each voxel is caused by the emitted rays whose AOIs are smaller than $\theta_{eff,lb}$. Meanwhile, the duplicated voxels do not appear in Figure 3b. As the incident lights on the waveguide are almost collimated due to the large depths of voxels ($|z_v| = 4000$ mm), the out-coupled lights have the same curvature of wave-front regardless of TIRs. This makes the observer perceive a single imaged voxel without the duplicated ones.

For the comprehensive analysis of the voxel duplication problem according to the virtual depths, we adopted the standard deviation (STD) among the angular positions of observed voxels, as defined in Equation (7).

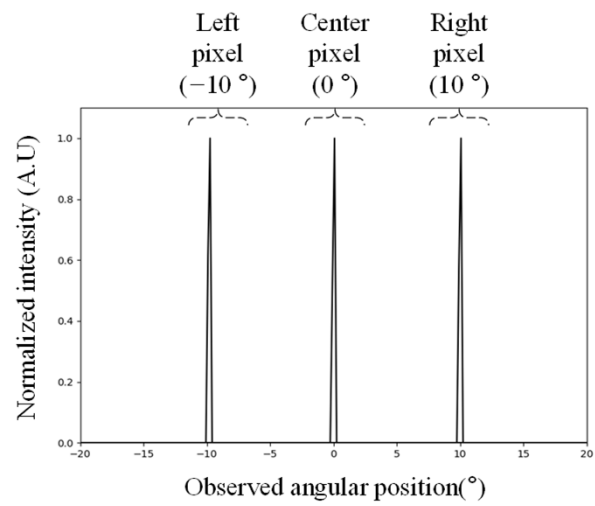
$$\delta_z = \frac{1}{K} \sum_{k=1}^K \sqrt{\frac{\sum_{r=1}^R \left(P_{k,r} - \frac{1}{R} \sum_{r=1}^R P_{k,r} \right)^2}{R}}, \tag{7}$$

where K , R , and $P_{k,r}$ denote the number of voxels, sampling number of rays for each voxel, and observed angular position for the k -th voxel with the r -th ray, respectively. As the number of duplicated voxels and angular distance among them determine δ_z , the evaluation metrics of Equation (7) allow the comprehensive analysis of the voxel duplication problem for each depth.

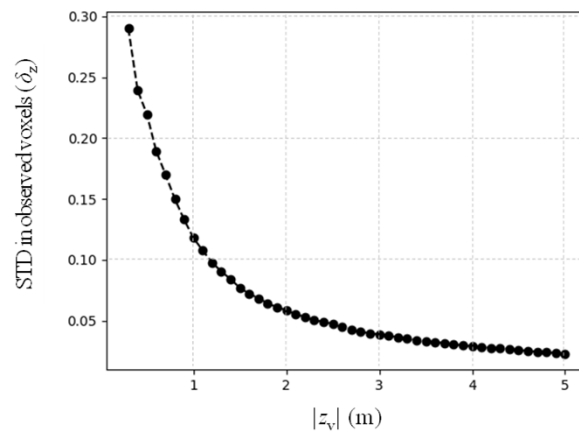
Figure 3c analyzes the changes in δ_z according to the represented depths, where z_v changed from -300 mm to -5000 mm, considering the typical use case of NEDs. For each depth, we assumed 1000 numbers of voxels with the large emission angle and field of view of 40° . When we represented the voxels in the near depth plane, the increase in the number of duplicated voxels and angular distance among them resulted in high δ_z . Meanwhile, for the voxels in the far depth plane, the distance among the duplicated voxels may become unnoticeable for the observer, such that δ_z in Figure 3c significantly decreases.



(a)



(b)



(c)

Figure 3. Simulation results for the observation case of voxels through the holographic waveguide: (a) $z_v = -400$ mm case, (b) $z_v = -4000$ mm case, and (c) the comprehensive analysis for the voxel duplication problem according to the represented depths using the evaluation metrics (δ_z).

2.2. Emission Angle Adjustment for Voxels Using InIm

In this section, we propose an adjustment method for the emission angle profile of each voxel in order to prevent the voxel duplication problem. For adjusting and optimizing the emission angle of voxels, we adopted the InIm technique, which is the representative autostereoscopy to provide the volumetric 3D images [19,20]. The InIm technique provides the correct depth cues, including the accommodation response for the human eye, as reported in Refs. [21,22]. For the subjects in these studies, 3D objects generated from the InIm system induced the correct accommodation response, which was similar to that of real objects with the same distance.

In the InIm, the directional rays synthesize and integrate the voxels. The relative position between the pixels in EIs and lenslets determines the propagation angle of each directional ray. Hence, the InIm can control the emission angle profile of voxels by applying the proper compensation method on the EIs. In this paper, sub-regions of EIs corresponding to the duplicated voxels are masked, in order to restrict the emission angle of voxels.

Figure 4 presents a schematic of the proposed system to solve the voxel duplication problem. In the proposed system, a holographic waveguide is combined with an InIm based on a lenslet-array. The InIm system reconstructs the voxel with the depth of $|z_v|$. Each lenslet in the InIm system generates ray bundles corresponding to the emission angle within the certain directional range. The ray bundles from the multiple numbers of lenslets synthesize the whole emission angle of voxels. Consequently, if we mask the sub-regions of EIs, which correspond to the emission angle exceeding the EAR, the voxel duplication problem can be alleviated.

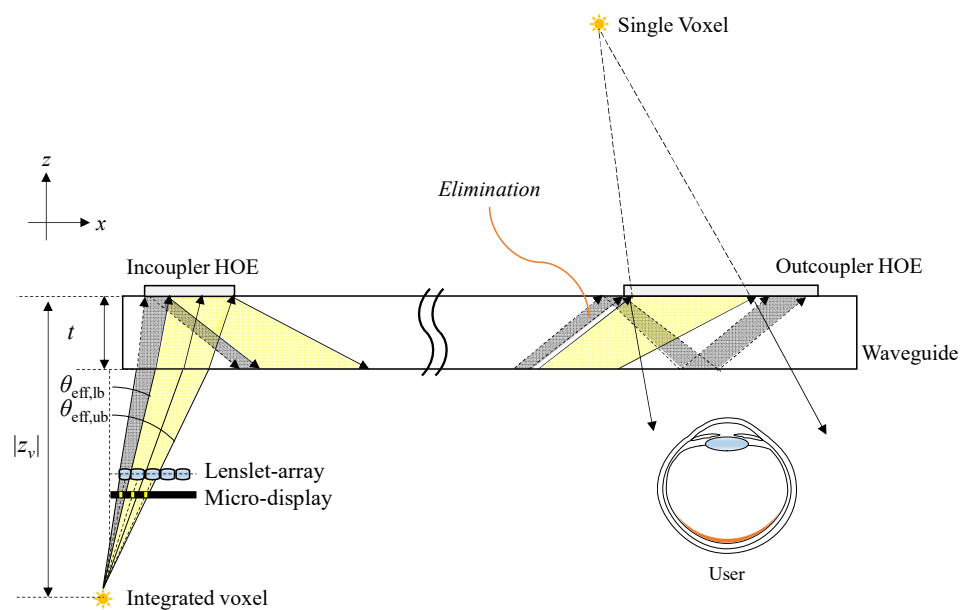


Figure 4. The principles of emission angle adjustment method using the InIm system for solving the voxel duplication problem.

Figure 5a depicts a detailed view of the InIm system. Supposing each lenslet of the lenslet-array has a pitch of p_l , and the integrated voxel V_{InIm} is located at (x_{InIm}, z_{InIm}) , when the origin of coordinate is at the center of lenslet-array, We assumed that the lenslet-array is composed of odd numbers of elemental lenslets, so that the center lenslet is placed at the origin of coordinate. In Figure 5a, three elemental lenslets, from the i -th to the $(i + 2)$ -th ones (when i is the integer), reconstruct the voxel (V_{InIm}) with the emission angle of $\theta_{e,InIm}$.

For the i -th lenslet from center, the upper and lower bounds for the emission angle of voxel are derived as below.

$$\theta_{InIm,i,ub} = \tan^{-1} \left(\frac{x_{InIm} - (C_{l,i} - 0.5p_l)}{z_{InIm}} \right), \tag{8}$$

$$\theta_{InIm,i,lb} = \tan^{-1} \left(\frac{x_{InIm} - (C_{l,i} + 0.5p_l)}{z_{InIm}} \right), \tag{9}$$

where $\theta_{InIm,i,ub}$ and $\theta_{InIm,i,lb}$ represent the upper and lower bounds for the emission angle of the voxel generated by the i -th elemental lenslet, respectively. $C_{l,i}$ denotes the center position of the i -th elemental lenslet, where $C_{l,i} = i \cdot p_l$ for the lenslet-array in Figure 5a. For example, the center of the 1st lenslet in Figure 5a is placed at the x coordinate of $C_{l,1} = p_l$.

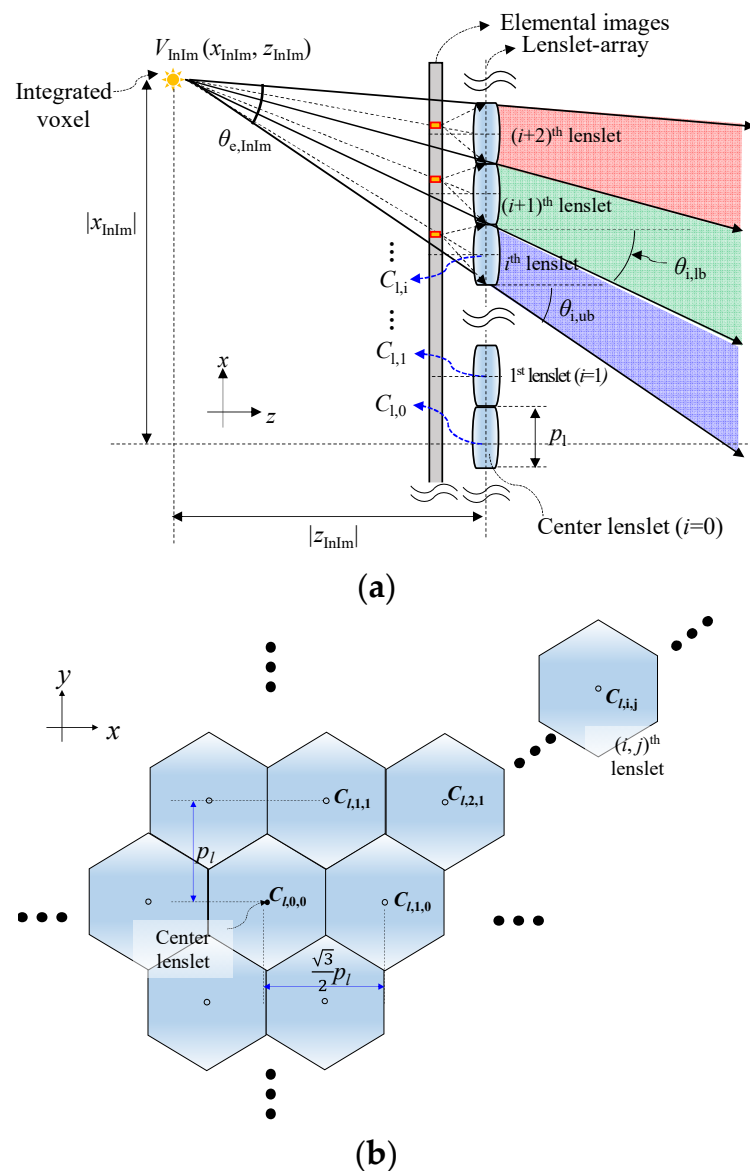


Figure 5. The schematic diagram for the emission angle construction of voxels in the InIm system: (a) the emission angle formation of integrate voxel in the InIm with the symmetrically arranged lenslet-array, and (b) the diagram for the arrangements and coordinates of lenslet center in the hexagonal lenslet-array.

If we mask a pixel in the EIs under the i -th lenslet in Figure 5a, the emission angle of integrated voxel ($\theta_{e,InIm}$) decreases by the amount of $\theta_{i,ub} - \theta_{i,lb}$. This alters the upper bound of the emission angle of the voxel from $\theta_{i,ub}$ to $\theta_{i+1,ub}$ ($=\theta_{i,lb}$), and prohibits the emitted light by exceeding the EAR. Consequently, the restricted emission angle of the integrated voxels using the masked EIs solves the voxel duplication problem in the holographic waveguide.

In the experiments in Section 3.2, we adopted a hexagonal lenslet-array, which is widely used for the InIm system to enhance 3D image quality [20,23,24]. The hexagonal lenslet-array typically has the hexagonal arrangements of lenslets, as shown in Figure 5b. In a two-dimensional schematic of hexagonal lenslet-array in Figure 5b, we supposed that the origin of the coordinate lies at the center of the lenslet-array. For the i -th lenslet in the horizontal direction and j -th in the vertical direction from the center lenslet, the center position is expressed as follows:

$$\begin{cases} C_{l,i,j,x} = \frac{\sqrt{3}}{2} \left(i + (-1)^{j+1} \frac{1}{4} - \frac{3}{4} \right) p_l \\ C_{l,i,j,y} = \frac{3}{4} p_l \times j \end{cases}, \tag{10}$$

where $C_{l,i,j,x}$ and $C_{l,i,j,y}$ represent x and y coordinates for the center position of the (i, j) -th lenslet. Similar to the case of the symmetrically arranged lenslet-array in Equations (8) and (9), the upper and lower bounds for the emission angle of voxel are expressed as Equation (11).

$$\begin{cases} \theta_{InIm,i,j,x} = \tan^{-1} \left(\frac{x_{InIm} - (C_{l,i,j,x} \pm \frac{\sqrt{3}}{4} p_l)}{z_{InIm}} \right) \\ \theta_{InIm,i,j,y} = \tan^{-1} \left(\frac{y_{InIm} - (C_{l,i,j,y} \pm \frac{1}{2} p_l)}{z_{InIm}} \right) \end{cases}, \tag{11}$$

where the plus sign and minus sign in Equation (11) represent the lower and the upper bounds for the emission angle of voxel by the (i, j) -th elemental lenslet, respectively. Since the hexagonal lenslet has the different pitch of lenslets in the horizontal and vertical directions, the emission angles are different according to the axis. Note that the pitch of the lenslet-array determines the minimum units for adjusting the emission angle in the proposed method. For the fine control in the emission angle of voxels to satisfy the EAR of holographic waveguide, the lenslet-array with a small pitch is preferred. Otherwise, the adjusted emission angle using the proposed method may lead to a mismatch with the EAR, which decreases the voxel brightness and observable area for the holographic waveguide.

3. Results

3.1. Fabrication of Full-Color Holographic Waveguide

For the experimental verification of the proposed method, we fabricated a thin holographic waveguide with the thickness of 5.0 mm. The in-coupler and out-coupler had symmetric volume gratings, in order to compensate for the chromatic dispersion of represented images [12], and the grating slanted angle (ζ) was selected to be 27.5° . A schematic diagram and picture of optical recording setup for the HOEs are provided in Figure 6a,b, respectively. Since a reference wave for the HOE couplers had to satisfy the TIR conditions, we used an additional glass prism and index matching oil in the recording process. In addition, in order to maximize the DEs of holographic waveguide, three layers of photopolymers were stacked on the waveguide for each coupler. We used the photopolymer film of Geola Digital Ltd. (Lithuania), which can be used for the lasers within the wavelength range from 440 nm to 680 nm.

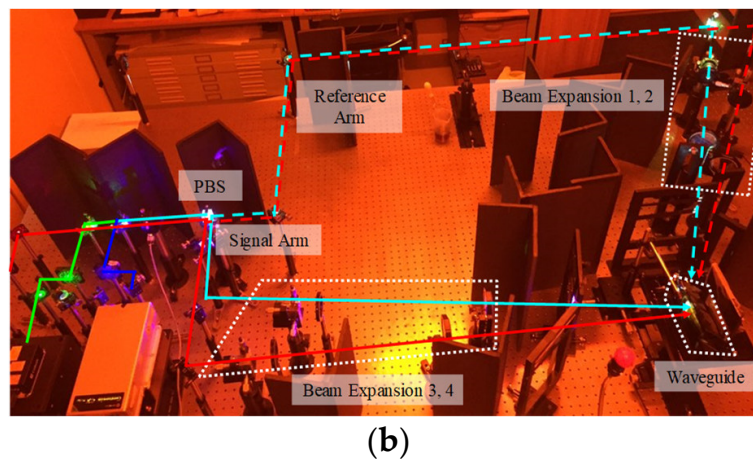
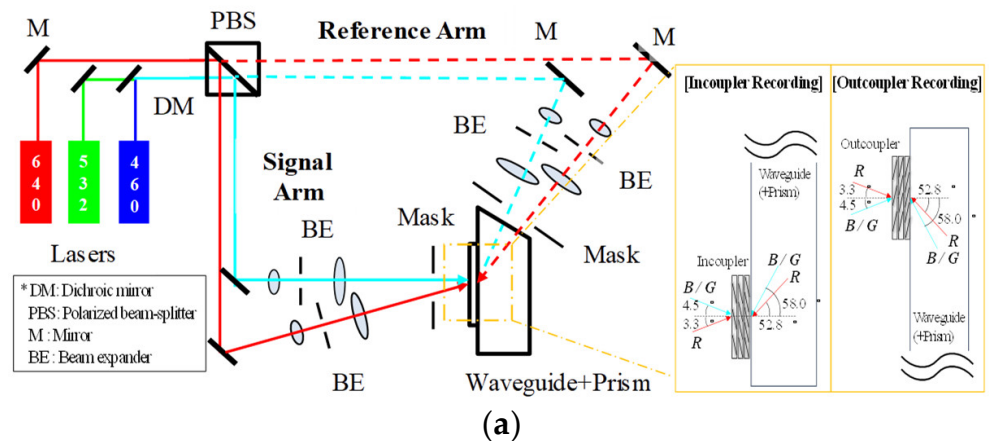


Figure 6. Experimental setup for recording HOEs: (a) the schematic, and (b) the picture of optical setup for recording the HOE couplers on the holographic waveguide.

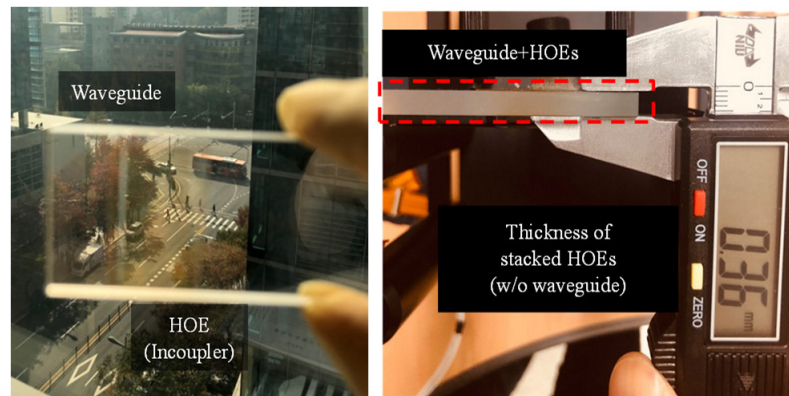
In the recording process, three lasers were controlled separately for recording full-color HOEs in the time-sequential method. While each laser illuminated the photopolymer for recording the interference patterns, we blocked the beam paths of other lasers. After each laser recorded the interference patterns, the photopolymer was fixed by using the ultraviolet (UV) light. Additionally, we laminated new photopolymer films on it to record the volume grating using another laser. For the reference beam path, the AOI on the photopolymer was set to be 58.0° for 460 nm and 532 nm, and 52.8° for 640 nm. For a signal path, the AOI on the photopolymer was set to be -4.5° for 460 nm and 532 nm, and 3.3° for 640 nm, as shown in Figure 6b. We carefully designed the AOI for each laser by considering a wavelength deviation between the recording and displaying setups, as presented in Refs. [17,25]. Other detailed specifications for the fabrication process of the holographic waveguide are listed in Table 1.

A picture of Figure 7a shows the high transparency of the fabricated waveguide, where we could view the real-world scene clearly through the HOE coupler. Although the three layers of photopolymers were stacked on the waveguide for the high DEs, the total thickness of HOE couplers was only 0.36 mm. Figure 7b presents a spectral transmittance of the fabricated HOE coupler, which was measured by a spectrometer (Flame-S-UV-VIS of Ocean Optics Inc., Amersham, UK). For measuring the transmittance spectrum, a probe light of the spectrometer was normally incident on the HOE coupler. The averaged transmittance in the visible spectrum (from 400 nm to 700 nm) was 74.0%, so that the fabricated coupler permitted the see-through properties of the holographic waveguide, as shown in Figure 7a. The full width at half maximum (FWHM) in the spectral response of HOE couplers was 9 nm, 11 nm, and 12 nm for blue, green, and red colors, respectively.

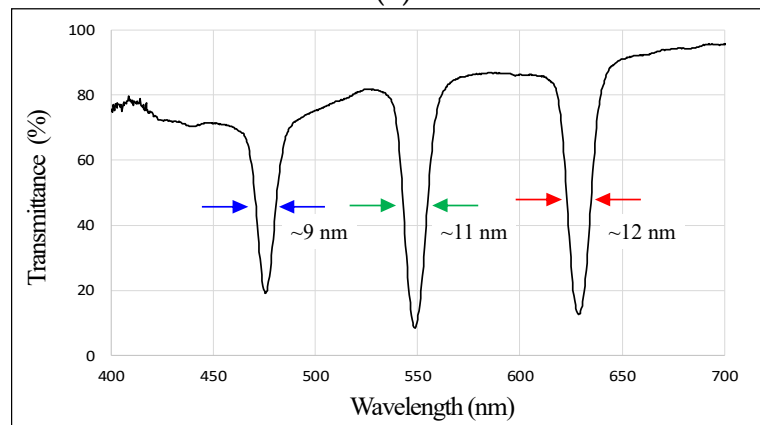
Table 1. Experimental specifications for fabricated holographic waveguide.

Items		Specifications	
Waveguide	Dimension Material	105.0 mm × 34.0 mm × 5.0 mm BK7	
HOEs	Dosage	31.0 mJ/cm ² (460 nm) 21.4 mJ/cm ² (532 nm) 17.2 mJ/cm ² (640 nm)	
	DE ¹ (in-coupler)	72.3% (460 nm) 78.0% (532 nm) 72.0% (640 nm)	
		DE (out-coupler)	73.3% (460 nm) 75.1% (532 nm) 72.9% (640 nm)
			Size
	Distance between in-coupler and out-coupler		62.5 mm
	Thickness		0.36 mm

DE was calculated using the power ratio between diffracted (1st order) and incident laser beam.



(a)



(b)

Figure 7. Characteristics of fabricated HOE couplers: (a) the fabricated waveguide sample with three layers of photopolymers, and (b) the transmittance spectrum of fabricated HOE coupler, when the probe wave was normally incident on the photopolymer.

3.2. Displaying Experiments for Representing Voxels

Figure 8 shows preliminary experimental results to verify the effect of emission angle adjustment for the voxels in the holographic waveguide. An InIm system was composed of an organic light-emitting diode (OLED) micro-display and a hexagonal lenslet-array

with 1 mm of lenslet pitch. We generated two sets of EIs for a small dice object in front of the waveguide with and without the proposed method, respectively. We presented the EIs in the upper parts of Figure 8. As shown in the captured images through the waveguide of Figure 8a, the conventional EIs did not only generate intended 3D images of dice, but also ghost images of dice. However, in Figure 8b, sub-regions of EIs were properly masked according to the principles of Section 2.2, so that pixels in the EIs corresponding to the ghost images were set to be black. The observed images through the waveguide in Figure 8b verified the effect of the proposed method, as the duplicated virtual images disappeared. In the normalized intensity profiles along the center row of the captured images in Figure 8, the peak intensity of the duplicated voxel was 0.256 in the proposed method, while it was 0.602 in the conventional method. Hence, by masking the EIs, the proposed method resulted in a reduced crosstalk in the observed voxels by 2.35 times, while the intended voxels hardly showed the degradation in image quality.

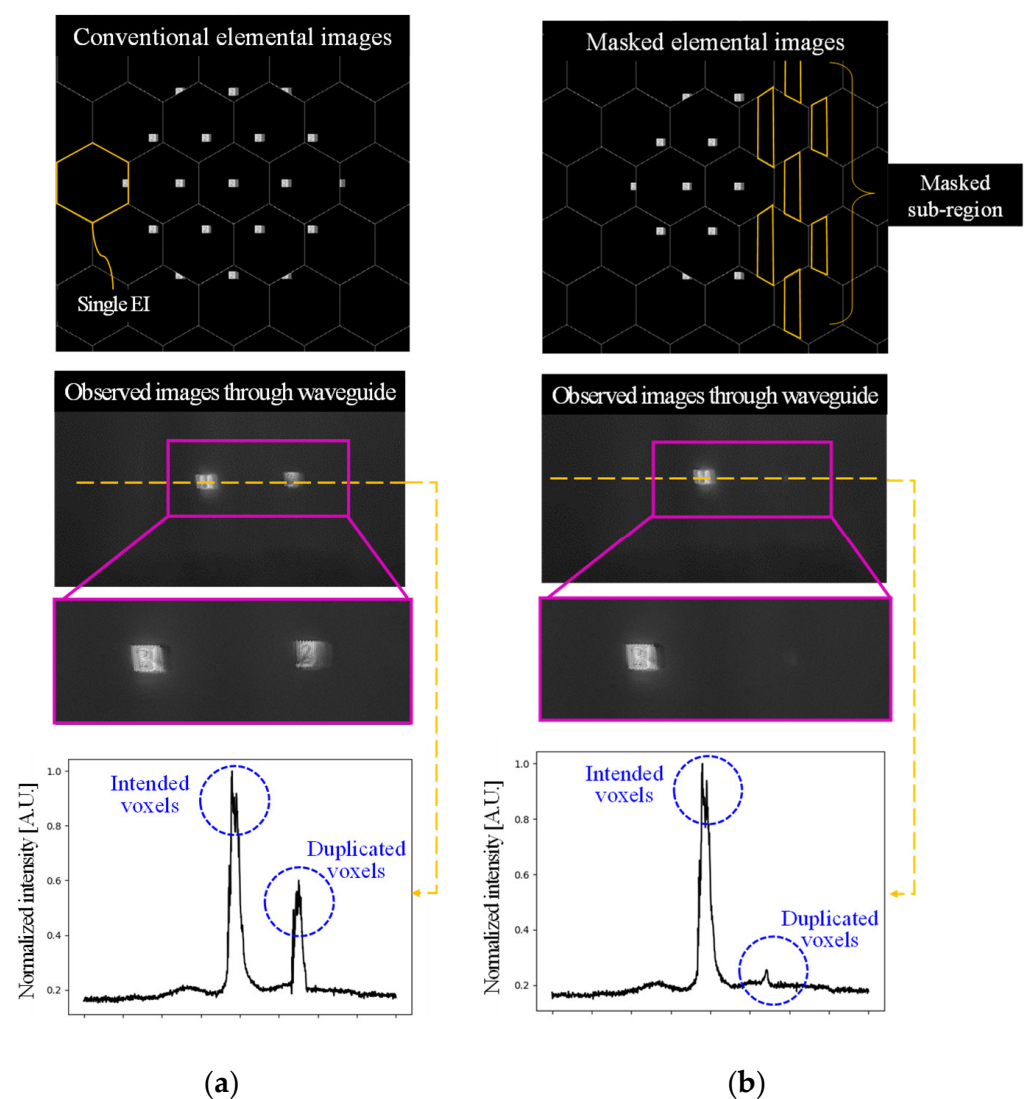
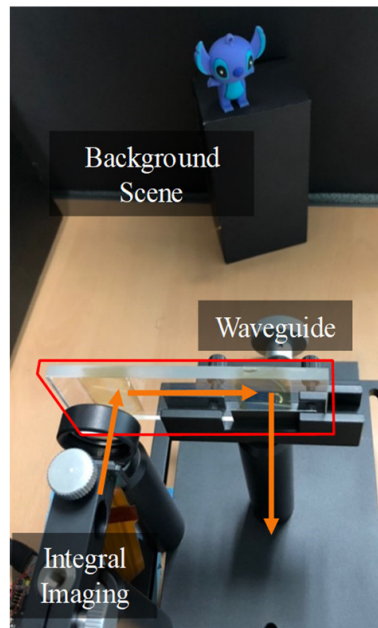
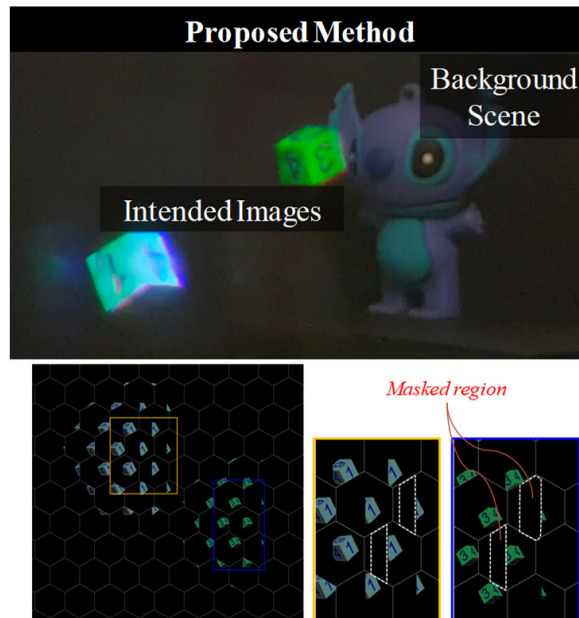


Figure 8. Preliminary experiments using the small dice object: we generated the EIs for the virtual depth of 400 mm (a) without, and (b) with applying the proposed method to solve the voxel duplication problem. The observed images through the holographic waveguide were captured, and the normalized intensity profiles along the dashed line at the center row of captured images are presented in the lower parts of the figure.

Figure 9a shows full-color displaying experiments. An InIm system was built using a micro-OLED display and 1 mm pitch lenslet-array. We placed a relay lens with a focal length of 30 mm between the InIm system and holographic waveguide, in order to enlarge the virtual depth of integrated voxels [26]. Table 2 presents other detailed specifications of displaying experiments. In the experimental configuration, the emitted light from a center voxel underwent the 10th or 12th number of TIRs until extraction. We eliminated the light that was extracted after the 12th TIR by applying the proposed method.



(a)



(b)

Figure 9. Cont.

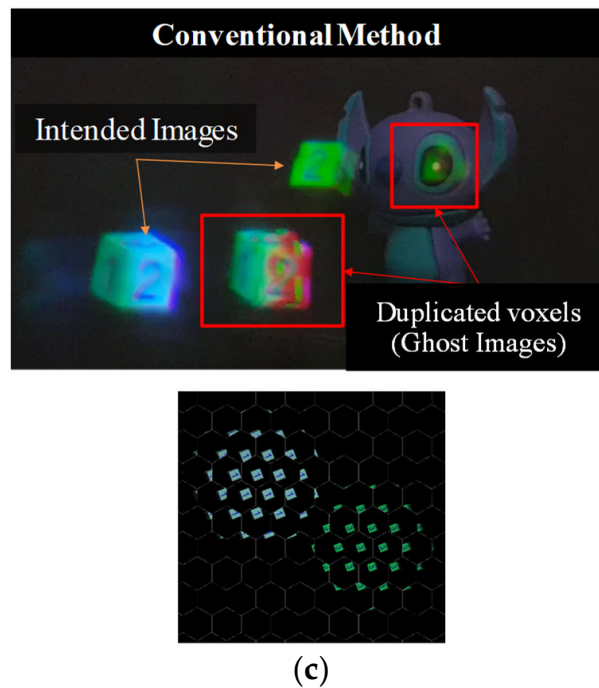


Figure 9. The full color displaying experiments using the OLED-based InIm system and holographic waveguide: (a) experimental setup for verifying the proposed method, and the resultant 3D images with their EIs (b) with and (c) without applying the proposed method. The EIs used for the displaying experiments are presented below the observed AR images.

Table 2. Experimental specifications for the displaying experiments using the holographic waveguide and InIm system.

Items		Specifications
Micro-display	Resolution	1920 × 1080
	Pixel pitch	8.3 μm
	Size	15.8 mm × 8.99 mm
Lenslet-array (Hexagonal)	Pitch	1 mm
	Focal length	3 mm
Relay Lens	Diameter	1 inch
	Focal length	30 mm

Figure 9b,c present the experimental results with their EIs. In the conventional method of Figure 9c, the intended 3D images and duplicated ones appeared at the same time. However, as shown in Figure 9b, the proposed method successfully removed the duplicated images, and displayed only the intended 3D images. The lower parts of Figure 9b show the EIs with the masked sub-regions which result in the voxel duplication problem. In addition, a background object verified the see-through properties of the fabricated system, which is viewable through the holographic waveguide with high transparency over 70%.

4. Discussion

The imaging characteristics of waveguides were investigated to represent the voxels with the broadband spectrum, where the incident light on the waveguide is non-collimated. Although we presented the analysis and experimental results by focusing on the holographic waveguides, the principles of the proposed method can be extended to other types of waveguide technologies. As discussed in Section 2, the voxel duplication problem arises from the large and non-optimized emission angle of the voxel, and the geometrical relationship between the waveguide and couplers. Hence, the analysis of voxel duplication

in Section 2 is still valid for other types of waveguide-based NEDs, such as the waveguides with prism-arrays-based couplers or reflective couplers [7,8].

Figure 10 presents a detailed configuration of image formation in the experiments of Figure 9, in order to analyze the design parameters of the InIm system with the relay lens. The InIm system has the central depth plane (CDP), where one can achieve the minimum spot size for the integrated voxels. The expressible depth range for the volumetric 3D images in the InIm is located around the CDP, and it is defined by the tolerable limit of image quality [19]. The limit for the expressible depth range is called the marginal depth plane, as presented in Figure 10a. By adopting the relay lens in front of the typical InIm system, it is possible to enlarge the CDP, so that the virtual images with long distances can be represented. When we denote the focal lengths of the lenslet-array and relay lens as f and f_{Relay} , respectively, the relayed CDP is expressed as Equation (12).

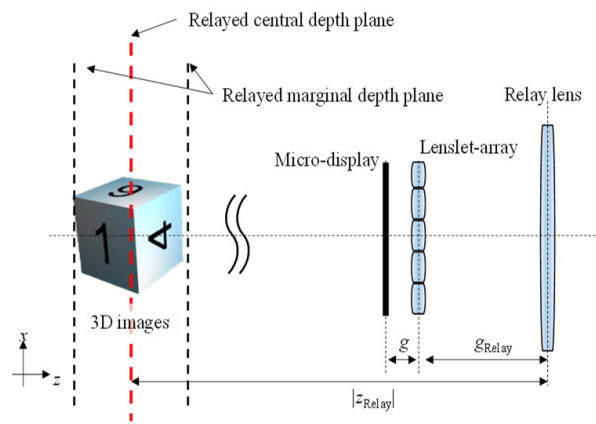
$$|z_{Relay}| = \left| f_{Relay} + \frac{f_{Relay}^2}{f^2/(f-g) - (f + f_{Relay} - g_{Relay})} \right|, \quad (12)$$

where $|z_{Relay}|$ denotes the distance of relayed CDP from the relay lens, g denotes the distance between the micro-display and lenslet-array, and g_{Relay} is the distance between the relay lens and the lenslet-array. Note that the z_{Relay} for NEDs is typically a negative number. Figure 10b presents the achievable range of $|z_{Relay}|$ by considering the specifications of lenslet-array in our experiments. We conducted the simulation with an f_{Relay} of 30 mm. By appropriately selecting the g and g_{Relay} , the location of the CDP is controllable. In our system, to represent the virtual objects at the near distance by considering the typical AR use case, the design parameters were selected to provide the voxels at 400 mm in front of the observers.

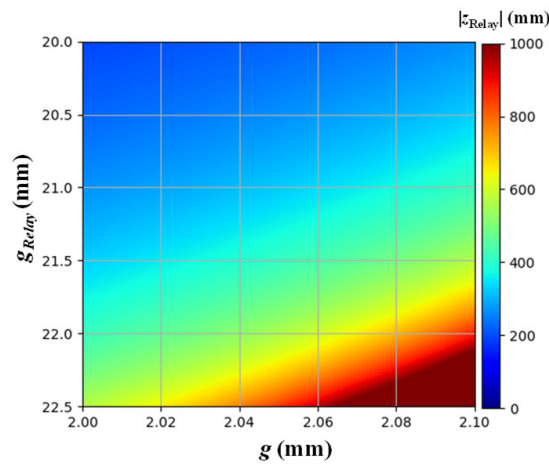
Within the expressible depth range defined by the relayed marginal depth planes in Figure 10a, the InIm system provides the voxels at different depth planes. Figure 10c shows the camera-captured images of the InIm system used in the experiments of Section 3.2. We generated EIs with two images at different depth planes (the letters “3” at the near depth plane, and the letter “4” at the far depth plane), and captured the observed images through the relay lens and InIm display. In the upper figure of Figure 10c, with the camera focus at the near depth plane, the integrated images of letters “3” and “4” showed focused and blurred images, respectively. Meanwhile, when we changed the camera focus to the far depth plane, the letters “3” and “4” showed blurred and focused images, respectively. Although we used the relay optics for the InIm system to enlarge the virtual depth plane, the experimental results in Figure 10c still had a limited depth range. This is due to the focusing errors of the lenslet-array and overlapping of the imaged pixels, as analyzed in Ref. [27]. For further extension of the expressible depth range, one can implement multiple (relayed) CDPs using a vari-focal lenslet-array or focus tunable relay lens in the InIm system, as proposed in Refs. [28,29].

The capability of representing the voxels and providing the correct depth cues is the important features for the NEDs, as the needs for the comfort and the usage time of the NEDs increase. In Table 3, we compared the proposed method and previous research for the NEDs using the holographic waveguide. As experimentally verified in this paper, the proposed method successfully provides 3D images without the voxel duplication problem, although we used the broadband and non-collimated light for the display source. Thus far, most studies on holographic waveguides have presented virtual images at optical infinity with a fixed and single-depth plane, since they used the conventional flat-panel displays with collimation optics [10,12]. When the holographic displays were adopted as the display sources [14,15], the small field of view in the holographic images did not suffer from the voxel duplication problem. However, if the holographic displays with the large field of view become available and used for the holographic waveguide, the voxel duplication problem may occur. In this case, one needs to optimize the hologram patterns to adjust the reconstructed wave-front of 3D objects, so that each voxel has the emission angle within the

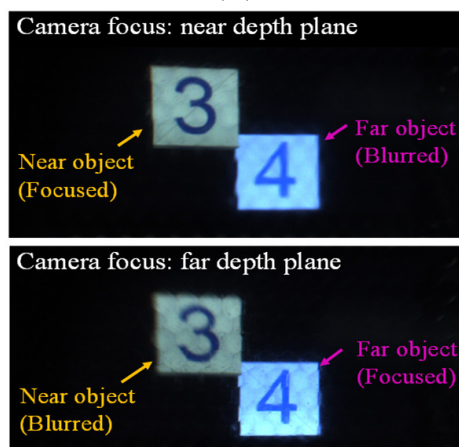
EAR. We believe that the proposed method, which adopts the concept of emission angle adjustment, is a promising technique for the various optical implementations of NEDs with mitigating the VAC problems.



(a)



(b)



(c)

Figure 10. The design parameters and depth representation properties of implemented InIm system: (a) the geometry of InIm system with the relayed CDP, (b) the simulated variation of $|z_{Relay}|$ according to the gap parameters in the InIm, and (c) the captured images for the relayed InIm system with the different camera focus.

Table 3. Comparison among the proposed method and previous research for the NEDs based on holographic waveguide.

Method	Display Source	Color	Voxel Representation
Proposed method	OLED + lenslet-array (Broad-band source)	Full-color	Supported
Virtual images at optical infinity (Refs. [10,12])	Flat-panel display + Collimation optics (Broad-band source)	Full-color	Not supported
Holographic display (Refs. [14,15])	Phase modulator + Collimated laser	Monochrome	Supported

5. Conclusions

In this paper, we analyzed the imaging characteristics of holographic waveguides for the non-collimated light emitted from the arbitrary voxel, and investigated the condition of the voxel duplication problem. In order to prevent the image crosstalk arising from the voxel duplication, we proposed the emission angle adjustment method for each voxel using the InIm and masked EIs. In the proposed method, the sub-regions of EIs corresponding to the duplicated voxels were masked, so that the optimized emission angle of voxels provided 3D images without the voxel duplication problem. In the experimental verification, the combined system of InIm and holographic waveguide with the thickness of 5.0 mm was implemented. For the holographic waveguide, the HOEs were fabricated using three layers of photopolymers, and showed high DEs of 72.8%, 76.6%, and 72.5% for 460 nm, 532 nm, and 640 nm lasers, respectively. The overall transmittance in the visible spectrum was over 74.0%. By applying the proposed method, the full-color displaying experiments successfully provided the see-through 3D contents without the ghost images due to the voxel duplication problem.

Author Contributions: Conceptualization, writing, visualization, investigation, supervision, resources, funding acquisition, and project administration, J.Y.; methodology, formal analysis, and data curation, Y.S. and K.C. All authors have read and agreed to the published version of the manuscript.

Funding: This work was supported by the Institute of Information & communications Technology Planning & Evaluation (IITP) grant funded by the Korea government (MSIT) (no. 2020-0-00088; development of thin lens and light weight projection engine technologies for AR devices).

Informed Consent Statement: Not applicable.

Data Availability Statement: All data generated or analyzed during this study are included in this published article.

Conflicts of Interest: The authors declare no conflict of interest.

References

1. Cakmakci, O.; Rolland, J. Head-worn displays: A review. *J. Disp. Technol.* **2006**, *2*, 199–216. [\[CrossRef\]](#)
2. Zhang, Y.; Fang, F. Development of planar diffractive waveguides in optical see-through head-mounted displays. *Precis. Eng.* **2019**, *60*, 482–496. [\[CrossRef\]](#)
3. Hua, H.; Hu, X.; Gao, C. A high-resolution optical see-through head-mounted display with eyetracking capability. *Opt. Express* **2013**, *21*, 30993–30998. [\[CrossRef\]](#)
4. Yoo, C.; Chae, M.; Moon, S.; Lee, B. Retinal projection type lightguide-based near-eye display with switchable viewpoints. *Opt. Express* **2020**, *28*, 3116–3135. [\[CrossRef\]](#) [\[PubMed\]](#)
5. Jang, C.; Bang, K.; Moon, S.; Kim, J.; Lee, S.; Lee, B. Retinal 3D: Augmented reality near-eye display via pupil-tracked light field projection on retina. *ACM Trans. Graph.* **2017**, *36*, 1–13. [\[CrossRef\]](#)
6. Cheng, D.; Wang, Y.; Xu, C.; Song, W.; Jin, G. Design of an ultra-thin near-eye display with geometrical waveguide and freeform optics. *Opt. Express* **2014**, *22*, 20705–20719. [\[CrossRef\]](#) [\[PubMed\]](#)
7. Zhang, W.; Wang, Z.; Xu, J. Research on a surface-relief optical waveguide augmented reality display device. *Appl. Opt.* **2018**, *57*, 3720–3729. [\[CrossRef\]](#) [\[PubMed\]](#)
8. Xu, M.; Hua, H. Methods of optimizing and evaluating geometrical lightguides with microstructure mirrors for augmented reality display. *Opt. Express* **2019**, *27*, 5523–5543. [\[CrossRef\]](#)
9. Kress, B.C.; Cummings, W.J. *Optical Architecture of Hologens Mixed Reality Headset*; SPIE: Brussels, Belgium, 2017; Volume 10335, p. 103350K.

10. Piao, M.-L.; Kim, N. Achieving high levels of color uniformity and optical efficiency for a wedge-shaped waveguide headmounted display using a photopolymer. *Appl. Opt.* **2014**, *53*, 2180–2186. [[CrossRef](#)]
11. Shishova, M.; Zherdev, A.; Lushnikov, D.; Odinkov, S. Recording of the multiplexed Bragg diffraction gratings for waveguides using phase mask. *Photonics* **2020**, *7*, 97. [[CrossRef](#)]
12. Yoshida, T.; Tokuyama, K.; Takai, Y.; Tsukuda, D.; Kaneko, T.; Suzuki, N.; Anzai, T.; Yoshikaie, A.; Akutsu, K.; Machida, A. A plastic holographic waveguide combiner for light-weight and highly-transparent augmented reality glasses. *J. Soc. Inf. Disp.* **2018**, *26*, 280–286. [[CrossRef](#)]
13. Su, W.-C.; Zhou, S.-K.; Lin, B.-S.; Lin, W.-K. Simplified Aberration Analysis Method of Holographic Waveguide Combiner. *Photonics* **2020**, *7*, 71. [[CrossRef](#)]
14. Yeom, H.-J.; Kim, H.-J.; Kim, S.-B.; Zhang, H.; Li, B.; Ji, Y.-M.; Kim, S.-H.; Park, J.-H. 3D holographic head mounted display using holographic optical elements with astigmatism aberration compensation. *Opt. Express* **2015**, *23*, 32025–32034. [[CrossRef](#)] [[PubMed](#)]
15. Lin, W.-K.; Matoba, O.; Lin, B.-S.; Su, W.-C. Astigmatism and deformation correction for a holographic head-mounted display with a wedge-shaped holographic waveguide. *Appl. Opt.* **2018**, *57*, 7094–7101. [[CrossRef](#)] [[PubMed](#)]
16. Chang, C.; Bang, K.; Wetzstein, G.; Lee, B.; Gao, L. Toward the next-generation VR/AR optics: A review of holographic near-eye displays from a human-centric perspective. *Optica* **2020**, *7*, 1563–1578. [[CrossRef](#)]
17. Shen, Z.; Zhang, Y.; Weng, Y.; Li, X. Characterization and optimization of field of view in a holographic waveguide display. *IEEE Photonics J.* **2017**, *9*, 1–11. [[CrossRef](#)]
18. Lee, C.-K.; Lee, T.; Sung, H.; Min, S.-W. Analysis and design of wedge projection display system based on ray retracing method. *Appl. Opt.* **2013**, *52*, 3964–3976. [[CrossRef](#)]
19. Park, J.-H.; Hong, K.; Lee, B. Recent progress in three-dimensional information processing based on integral imaging. *Appl. Opt.* **2009**, *48*, H77–H94. [[CrossRef](#)]
20. Park, S.; Yeom, J.; Jeong, Y.; Chen, N.; Hong, J.-Y.; Lee, B. Recent issues on integral imaging and its applications. *J. Inf. Disp.* **2014**, *15*, 37–46. [[CrossRef](#)]
21. Kim, Y.; Kim, J.; Hong, K.; Yang, H.K.; Jung, J.-H.; Choi, H.; Min, S.-W.; Seo, J.-M.; Hwang, J.-M.; Lee, B. Accommodative response of integral imaging in near distance. *J. Disp. Technol.* **2012**, *8*, 70–78. [[CrossRef](#)]
22. Chen, C.; Deng, H.; Zhong, F.-Y.; Ji, Q.-L.; Li, Q. Effect of viewpoints on the accommodation response in integral imaging 3D display. *IEEE Photonics J.* **2020**, *12*, 7000414. [[CrossRef](#)]
23. Chen, N.; Yeom, J.; Jung, J.H.; Park, J.H.; Lee, B. Resolution comparison between integral-imaging-based hologram synthesis methods using rectangular and hexagonal lens arrays. *Opt. Express* **2011**, *19*, 26917–26927. [[CrossRef](#)] [[PubMed](#)]
24. Wen, J.; Yan, X.; Jiang, X.; Yan, Z.; Wang, Z.; Chen, S.; Lin, M. Comparative study on light modulation characteristic between hexagonal and rectangular arranged macro lens array for integral imaging based light field display. *Opt. Commun.* **2020**, *466*, 125613. [[CrossRef](#)]
25. Yeom, J.; Son, Y.; Choi, K.-S. Pre-compensation method for optimizing recording process of holographic optical element lenses with spherical wave reconstruction. *Opt. Express* **2020**, *28*, 33318–33333. [[CrossRef](#)]
26. Hong, J.; Yeom, J.; Lee, B. Enhancing angular sampling rate of integral floating display using dynamically variable apertures. *Opt. Express* **2012**, *20*, 10242–10255. [[CrossRef](#)]
27. Luo, C.-G.; Xiao, X.; Martínez-Corral, M.; Chen, C.-W.; Javidi, B.; Wang, Q.-H. Analysis of the depth of field of integral imaging displays based on wave optics. *Opt. Express* **2013**, *21*, 31263–31273. [[CrossRef](#)]
28. Shin, D.; Kim, C.; Koo, G.; Won, W.H. Depth plane adaptive integral imaging system using a vari-focal liquid lens array for realizing augmented reality. *Opt. Express* **2020**, *28*, 5602–5616. [[CrossRef](#)]
29. Huang, H.; Hua, H. High-performance integral-imaging-based light field augmented reality display using freeform optics. *Opt. Express* **2018**, *26*, 17578–17590. [[CrossRef](#)]